Journal of Non-Crystalline Solids 637 (2024) 123054

Contents lists available at ScienceDirect

Journal of Non-Crystalline Solids

journal homepage: www.elsevier.com/locate/jnoncrysol

Effects of UO_3 on the structure, thermal and chemical stability of borosilicate glass matrix

I. Tolnai [a], J. Osan [a], F. Pinakidou [b], Zs. Kovacs [c], M. Fabian [a,*]

[a] HUN-REN Centre for Energy Research, Konkoly Thege St. 29-33., Budapest 1121, Hungary
[b] Aristotle University of Thessaloniki, School of Physics, Thessaloniki 54124, Greece
[c] Department of Materials Physics, Institute of Physics, Eötvös Loránd University H-1117 Budapest, Pázmány Péter st. 1/a, Hungary

ARTICLE INFO

Keywords:
Borosilicate glass
Uranium oxidation state
Neutron diffraction
Reverse Monte Carlo simulation
Thermal characteristics
leaching test

ABSTRACT

The glass matrix of composition: $55SiO_2$–$10B_2O_3$–$25Na_2O$-5BaO-$5ZrO_2$ was incorporated with 10 to 40 wt% of UO_3 by melt quenching technique. Neutron diffraction and Reverse Monte Carlo simulations revealed that the borosilicate network consists of SiO_4, BO_3 and BO_4 units; upon adding 10 % UO_3 the B-O coordination increases from 3.08 to 3.86 and subsequently decreases with a further in increase in UO_3 content. X-ray absorption near edge and Extended X-ray absorption studies revealed that U exist in 5+ and 6+ oxidation states with U-O coordination numbers of 8 and 6 respectively. The thermal stability decreases and weight losses increases with the addition of UO_3 in the glass matrix, the sample with 30 wt% UO_3 has thermal stability comparable to that of matrix glass and exhibits lowest dissolution rate in water. Nanoindentation measurements showed that the microstructure of sample with 30 wt% UO_3 is 11 % weaker than that of the matrix glass.

1. Introduction

Immobilization of high-level radioactive waste (HLW) into a glass matrix by the vitrification process is a well-accepted technology that is being used worldwide [1,2]. Vitrification is an established technique to accommodate a wide range of long-lived radionuclides and it also ensures the highest degree of environmental protection [3]. Engineered barrier system (EBS) is part of a multi-barrier system responsible for the long-term safe storage of radioactive wastes isolated from the biosphere in a deep geological repository. The EBS itself comprises a variety of sub-systems such as the waste form (radioactive material immobilized in a host matrix), a corrosion-resistant and mechanically stable container, a buffer/sealing system, and plugs. The EBS must be designed so that it will work with the natural barriers to meet the regulatory limits [4,5]. Vitrification is the first barrier of the EBS in which way we could ensure the immobilization of the HLW materials. Many countries such as the US, Canada, Sweden, and Hungary also decided not to reprocess the spent nuclear fuel leaving it in interim storage while waiting for possible disposal (open fuel cycle), but some countries such as France, Russia, the UK and Japan reprocess their spent nuclear fuel to recover remaining uranium and plutonium to prepare new nuclear fuel and to reduce the radiotoxicity of the remained waste containing the fission products and minor actinides (closed fuel cycle) [6]. The spent nuclear fuel may still contain about 96 wt% of reusable material (U, Pu) to produce energy. The ultimate high-level radioactive waste (HLW) that remains after the reprocessing of spent nuclear fuel is today conditioned (vitrified) by dissolution at the atomic scale in highly durable glassy forms [7]. Nowadays borosilicate glasses are the first candidates for the immobilization of nuclear waste materials [8,9].

In this paper, the focus is on the structural changes and chemical durability of the uranium dopped matrix glasses prepared by vitrification processes by melting the mixture of the matrix glass with the waste form. The waste form in the studied case is simulated with uranium trioxide. The main challenge is to find the highest concentration that could be immobilized in this 5-component matrix glass form. Studies have been performed on different types of glass containing different forms of uranium (uranyl acetate, uranium trioxide), but with relatively low waste concentrations [10-12]. In laboratory conditions, we want to find the maximum UO_3 load where the basic requirements are also satisfactory.

The glass matrix sample was earlier synthesized and characterized [13] with the composition of glass forming-, modifying- and stabilizing oxides ($55SiO_2{\cdot}10B_2O_3{\cdot}25Na_2O{\cdot}5BaO{\cdot}5ZrO_2$ [mol %]). It is expected that this specific composition can immobilize significant amount of

* Corresponding author.
E-mail address: fabian.margit@ek.hun-ren.hu (M. Fabian).

https://doi.org/10.1016/j.jnoncrysol.2024.123054
Received 19 February 2024; Received in revised form 23 May 2024; Accepted 24 May 2024

actinides (U, Pu) in an amorphous structure that are generally able to dissolve a broad spectrum of radioactive waste of different activities. Borosilicate glasses are characterized by large glass-forming ability, good chemical, thermal, and radiation stability.

The study is focused on a borosilicate model waste glass series where the matrix glass was loaded with UO_3 at four concentrations from 10 to 40 wt%. To ensure the long-term containment performance of the waste glass, it is necessary to evaluate the thermo-physical-chemical properties and structural characteristics. Some of these properties, like glass transition temperature or chemical durability are essential data for HLW immobilization. The structure of glasses could change with the incorporation of UO_3, and the glass structure is studied by neutron diffraction measurements supported by the Reverse Monte Carlo simulation and by X-ray absorption fine structure spectroscopy.

Because the conditioned waste has to be kept by geological disposal in a deep underground repository following a multiple barrier containment approach [14,15], these glassy forms will constitute the first containment barrier. Therefore, long-term behavior - chemical durability - of the borosilicate model waste glass series was investigated by water leaching experiments and thermal stability (that simulates the self-irradiation nature of waste glasses) measurements. These were performed by leaching tests using Milli-Q Type 1 Ultrapure (MQ-water) and porewater [16,17], and thermal analysis methods. As Boda Clay Formation (BCF) is considered as the potential host rock system for the Hungarian HLW storage, synthetic porewater, model based on the characteristics of BCF was used in the leaching tests.

The present study provides new insights on the short-range structural properties, such as Si-O, Ba-O, B-O and U-O bond distances and coordination environments, U oxidation states in a series of U-loaded borosilicate glass. Further we have used our previous data obtained for matrix glass (referred to as REF sample) to understand the effects of uranium ions on the structural, thermal, mechanical and chemical dissolution properties of borosilicate glass [13].

2. Materials and methods

2.1. Synthesis and density measurement

The 6-component sodium borosilicate glass system, of composition: (100-x) wt% [$55SiO_2{\cdot}10B_2O_3{\cdot}25Na_2O{\cdot}5BaO{\cdot}5ZrO_2$] + x wt% UO_3 was synthesized with UO_3 at four concentrations ($x = 10$, 20, 30 and 40 wt%, denoted as MU10, MU20, MU30 and MU40, respectively) to investigate the changes in the atomic properties and the impact on the basic structure of the glass matrix following the incorporation of U ions. The $55SiO_2{\cdot}10B_2O_3{\cdot}25Na_2O{\cdot}5BaO{\cdot}5ZrO_2$ (mol %) composition is the matrix glass, denoted as REF. The samples were prepared using high-purity raw materials of analytical grade SiO_2, Na_2O, BaO, ZrO_2, B_2O_3 (Sigma-Aldrich, Budapest, Hungary) and UO_3 (Reactivul, Bucharest, Romania). B^{11} enriched B_2O_3 was used for glass synthesis, this enrichment minimized the impact of neutron absorption associated with the occurrence of ~20 atomic % of ^{10}B in natural boron. Through the application of the inductively coupled plasma mass spectroscopy technique, the ^{11}B isotope enrichment was determined to be 99.6 % [18]. For sample preparation, a high temperature electrical furnace was used with a platinum crucible for glass melting under atmospheric conditions. The batch mixture was melted at 1450 °C and the melt was held at this temperature for 2 h. Following this, the melt was cooled to 1200 °C and then quickly quenched by pouring it onto a stainless-steel plate. The disk shaped samples were ball-milled into fine powder using agate balls, and a particle size of 50 μm was achieved with a Retsch MM400 Mixer Mill.

The density of the bulk samples was measured with a pycnometer at 24±0.1 °C. MQ- water (Milli-Q Type 1 Ultrapure water) was used as the working liquid. Each sample underwent density measurements five times, yielding a standard deviation of 0.03 g·cm^{-3}. The density values of the glasses were 3.22±0.03 g cm^{-3}, 3.34±0.03 g cm^{-3}, 3.45±0.03 g cm^{-3}, and 3.52±0.03 g·cm^{-3} for MU10, MU20, MU30 and MU40 samples respectively.

2.2. Neutron diffraction measurements

Neutron diffraction (ND) measurements were conducted using the PSD diffractometer (λ_0 = 1.068 Å, Q = 0.45–9.8 $Å^{-1}$) [19] at the Budapest Neutron Centre (BNC) for the MU30 sample and at the 7C2 diffractometer at the Laboratoire Léon Brillouin (λ_0 = 0.726 Å, Q = 0.3–16 $Å^{-1}$) [20] in case of the MU10, MU20 and MU40 samples. Powder specimens weighing approximately 4–5 g each were placed in thin-walled cylindrical vanadium sample holders with diameters of 8 mm (PSD), and 6 mm (7C2). Corrections for detector efficiency, background scattering, and absorption effects were applied to the raw data. The total structure factor was computed using local software packages. A detailed presentation of the data evaluation was provided earlier [13].

2.3. Pair distribution function (PDF) calculation

The atomic pair distribution function, $g(r)$ of each sample was calculated by the Fourier sine transformation of the neutron interference function ($S(Q)-1$) amplified with Q i.e. $F(Q)=Q(S(Q)-1)$ by using the following formula:

$$g(r) = 1 + \frac{1}{2\pi^2\rho_o r}\int_{Qmin}^{Qmax} F(Q)M(Q)Sin(Qr)\ dQ \tag{1}$$

where, ρ_o is the atomic number density of the sample and $M(Q)$ is the Lorch modification function defined as:

$$\begin{aligned} M(Q) &= \frac{Sin(\Delta Q)}{\Delta Q}, \quad Q \le Q_{max} \\ &= 0 \qquad\qquad Q > Q_{max} \\ \text{and}\Delta &= \frac{\pi}{Q_{max}} \end{aligned} \tag{2}$$

Q_{max} =16.0 $Å^{-1}$ was used for calculating $g(r)$ for samples; REF, MU10, MU20 and MU40. However, Q_{max}=9.8 $Å^{-1}$ was used for the sample MU30 which was measured at lower Q_{max} value at the PSD beamline of BNC.

2.4. Short–range structure by RMC analysis

The Reverse Monte Carlo (RMC) simulation is a powerful technique to build large 3D structural models in accordance with experimental data, in particular total structure factors ($S(Q)$) obtained from diffraction experiments [21]. The $S(Q)$ data for neutron diffraction were simulated using the RMC++ code [22]. The RMC algorithm computes the one-dimensional partial atomic pair correlation functions, $g_{ij}(r)$, and employs inverse Fourier transformation to calculate the partial structure factors, $S_{ij}(Q)$, as follows:

$$S_{ij}(Q) = 1 + \frac{4\pi\rho_0}{Q}\int_0^{r_{max}} r\left[g_{ij}(r) - 1\right]\sin Qr\ dr \tag{3}$$

where ρ_0 and r_{max} are the atomic number density and the half-edge-length of the simulation box in the RMC calculation. The computer configuration is altered by randomly displacing atoms until the calculated $S(Q)$ aligns with the experimental data within the margin of experimental error.

The partial atomic pair correlation functions, denoted as $g_{ij}(r)$, were determined using the RMC method. The weighting factors, w_{ij}, and the partial structure factors, $S_{ij}(Q)$, were defined through the following equations:

$$w_{ij} = \frac{c_i c_j b_i b_j}{\left[\sum_i^k c_i b_i\right]^2} \tag{4}$$

$$S(Q) = \sum_{i,j}^{k} w_{ij} S_{ij}(Q) \tag{5}$$

where c_i, c_j are the molar fractions of the i^{th} and j^{th} components and b_i, b_j are their coherent neutron scattering lengths, Q is the momentum transfer or the scattering vector. In the studied glassy specimens $k = 7$ (number of different atoms in the sample) which corresponds to a total of 28 atom pairs based on $k(k+1)/2 = 28$. The neutron weighted factors for the cation-oxygen and oxygen-oxygen atomic pairs with the largest contribution to the ND are given in Table 1.

The initial setup during RMC runs involved a cubic simulation box filled with 10,000 randomly placed atoms. Atom swaps were only allowed if they met previously specified constraints. Atomic densities were derived from pre-established values, contributing the length of the box edges: 24.74 Å, 24.97 Å, 25.01 Å, and 25.46 Å for MU10, MU20, MU30, and MU40, respectively. During the RMC runs, two types of constraints were implemented: minimum inter-atomic (cut-off) distances and Si-O tetrahedral coordination constraints. The initial configuration's cut-off values were derived from our earlier findings, which were established for SiO_2—Na_2O [23], B_2O_3—Na_2O glasses [24], the matrix glass [13], and the matrix glass containing lanthanides [25].

2.5. X-ray absorption fine structure

Synchrotron radiation measurements were conducted at the B18 XAS beamline of the Diamond Light Source [26]. Spectra covering both X-ray absorption near-edge structure (XANES) and extended X-ray absorption fine structure (EXAFS) regions were acquired, utilizing a Si (111) monochromator around the L_{III} absorption edge of U. Glass samples, comprised of 13 mm diameter pressed pellets containing 18–28 mg cm^{-2} of uranium-containing glass with polyvinylpyrrolidone as the binder, were examined, the XAFS spectra were collected in transmission mode. Reference compounds UO_2 and UO_3 were similarly measured in the form of pressed pellets. All spectra were acquired at room temperature in ambient air. The Si(111) monochromator underwent tuning with energy steps of 0.5 eV both at the absorption edge and in the near-edge region, and a k-constant step of 0.03 $Å^{-1}$ in the extended region. Ionization chambers were used to monitor the intensity of both incoming and transmitted X-rays with 2 s dwell time per energy step, normalization of the detected intensity was performed with respect to the incident photon flux. To enhance the signal-to-noise ratio, multiple spectra were collected and subsequently merged for each sample. The energy scale calibration was conducted using reference Zr-foil with K absorption edge falling within the energy region of the U-L_{III} absorption edge.

The determination of uranium oxidation state in the borosilicate glass samples involved using linear combination fitting (LCF) within the XANES region. This process utilized reference spectra derived from model compounds: UO_2 for U^{IV}, UO_3 for U^{VI}, and U_3O_8 for 67 % U^{V} and 33 % U^{VI}. Extensive data processing, including background removal, normalization of XAFS spectra and LCF, was conducted using the Athena software Package [27]. EXAFS analysis involved the use of FEFF8.2 to calculate theoretical phase and amplitude functions for scattering paths, with curve fitting undertaken in both R- and k-space through the implementation of FEFFIT [28].

Table 1
Neutron-weighted factors, w_{ij} [%] of the matrix glass (REF) and the 7-component U-containing glass samples, focusing on X-O and O—O partial interatomic correlations.

Samples	Si-O	B-O	Na-O	Ba-O	Zr-O	U-O	O-O
	Neutron-weighted factors, w_{ij} [%]						
REF	18.68	10.32	12.24	1.58	3.68	–	39.95
MU10	16.79	9.77	13.29	1.81	2.62	2.03	40.46
MU20	15.65	9.11	12.39	1.72	2.44	4.84	40.79
MU30	14.4	9.33	10.81	1.66	4.13	6.20	40.78
MU40	14.06	8.25	11.19	1.54	2.22	8.76	41.11

2.6. Differential thermal analysis

Differential Thermal Analysis (DTA) measurements were performed on a SETARAM 92–16.18 DTA equipment with a TGA-92 set-up under Ar atmosphere. The DTA was calibrated by melting of high-purity In, Zn and Al metals. Each DTA scan consisted of a controlled heating with 10 °C/min constant heating rate from room temperature to 1500 °C and a subsequent instantaneous uncontrolled fast cooling of the sample down to room temperature. Baselines both heat flow and weight change signals were recorded by heating an empty Al_2O_3 sample holder with the same temperature program.

2.7. Leaching test

The chemical durability of the homogeneous glass waste form and the chemical evolution of the leaching solution were evaluated by calculating the normalized release and glass dissolution rate of silicate, boron and uranium using the equations specified in the ASTM C1285–21 protocol [29]. This analysis involved measuring the concentration of elements released into the leaching solution.

$$NL_i = \frac{c_i(sample)}{(f_i)\cdot\left(\frac{SA}{V}\right)} \tag{6}$$

$$NR_i = \frac{c_i(sample)}{(f_i)\cdot\left(\frac{SA}{V}\right)\cdot(t)} \tag{7}$$

where $c_i$is the concentration of element of interest in the given soaking water (g/l), $f_i$is the weight fraction of element of interest in the initial borosilicate glass (unitless), $\frac{SA}{V}$ is the surface area of the final waste form divided by the volume of the leachate (m^{-1}) and t is the duration of the experiment (days).

Both MQ-water and synthetic porewater was used as leaching solutions. The calculation of the modeled synthetic porewater chemistry was performed with the MINSORB geochemical speciation code and the Nagra/PSI 01/01 thermodynamic database [16,17]. Porewater chemistry was calculated at fixed p_{CO2} ($10^{-3.5}$ bar)/pH (8.0), in equilibrium with atmospheric p_{CO2}, and constrained by calcite, dolomite, and quartz saturation. Adjustments to Na^+ or Cl^- concentrations maintained charge neutrality, while Ca, Mg, Si, and C(IV) concentrations were defined within specified conditions [30]. The synthetic Boda porewater based on the characteristics of BCF and is referred as SBPW. The composition of SBPW is given in the Supplementary Table 1.

The 100 to 200-mesh size fraction of the crushed samples was used for the leaching test. The protocol was carried out in 304 L stainless steel cylindrical containers, with a laboratory oven maintaining the temperature at 90±1 °C. The calculated surface area to volume ratio (SA/V) was 1600 m^{-1} for all samples, assuming a cubic shape for the glass particles throughout the calculations. After 3, 7, and 10 days, the containers were opened, and the leachates were filtered through a 0.45 μm syringe filter. Subsequently, the leachates were acidified with cc. HNO_3 for inductively coupled plasma optical emission spectroscopy (ICP-OES) measurements using a Perkin Elmer Avio 200 ICP-OES apparatus.

2.8. Nanoindentation

The mechanical properties of the samples were investigated by an Anton Paar HIT300 nanoindenter. (Nano)hardness was measured with a Vickers tip applying a linear force up to 50 mN which was reached in 30

s. A hold time of 10 s was used before the unloading (also 30 s). The measurement was repeated for 19 and 17 times (neglecting the clearly wrong measurements) for the REF and sample MU30, respectively. The distance between the indentation points was 0.1 mm, which is larger than 30 times the maximal indentation depth (about 700 nm, 0.7 um); according to the ISO standard. Indentation moduli (*EIT*) and indentation hardness (*HIT*) were calculated by the Oliver-Pharr method, estimating a Poisson's ratio of $\nu = 0.2$ for both samples. Hardness is also presented in the traditional unit "Vickers".

3. Results and discussion

3.1. Glass structure by PDF and RMC analyses

Fig. 1 shows the *S(Q)* functions derived from ND and the *S(Q)* functions determined via RMC simulation (colored triangles: experimental *S(Q)*; black solid line: RMC calculation).

Fig. 2 gives the *g(r)* distributions of 4 glass samples containing varying amounts of UO_3. It is seen that the samples MU10, MU20 and MU40 show the first peak at 1.60 Å due to Si-O pairs and a shoulder at 1.43 Å is clearly visible due to B-O pair correlations in these 3 samples. The sample MU30 was measured at a lower real space resolution with $Q_{max} = 9.8\ \AA^{-1}$ and it shows the first peak centered at 1.46 Å due to strongly overlapping B-O and Si-O pair correlations. A clear shoulder at ~2.2 Å is visible in the *g(r)* distributions of the samples; MU10, MU20 and MU40 and is due to Na-O pair correlations. The shorter O—O distances (doublet in O—O distances is confirmed by RMC analysis discussed below) and the longer U-O bond lengths exhibit another shoulder at ~2.4 Å. The shorter U-O bond lengths occur at ~1.8 Å and these could not be resolved in *g(r)* and are strongly overlapping with Si-O peak.

The *g(r)* distributions of all samples show the second strong peak at ~2.6 Å due to both O—O distances and Ba-O bond lengths. The *g(r)* distribution represents the weighted sum of partial atomic pair correlations $g_{ij}(r)$, however the accurate calculation of B-O, Si-O, Na-O, U-O, Ba-O and O—O bond lengths and coordination numbers from the radial distribution function analysis is difficult due to strongly overlapping B-O, Si-O Na-O and U-O atomic pairs in *g(r)*. To accurately calculate the cation-oxygen bond lengths/distances and the coordination numbers, the partial atomic pair distribution functions, $g_{ij}(r)$ were determined from the RMC simulations of the neutron structure factors.

About 26 atomic configurations were obtained per sample using RMC calculations corresponding to close to 1500,000 approved atomic displacements within the simulation box. Based on the ND patterns the melt quenching sample preparation technique was deemed adequate, as no traces of crystalline phases could be detected, and the samples were found to be completely amorphous. The convergence of the RMC simulation is adequate, as the calculated data fits well with the experimental data (Fig. 1). Despite continuous changes in uranium concentration, no significant changes can be observed in the shape of structure factors of U-loaded sample series compared to the REF sample. The *S*(*Q*) functions obtained generally share similarities, with the most pronounced distinctions observed in the low *Q*-range, mostly between 1.4–2.2 $\AA^{-1}$. The RMC++ software is utilized to generate partial atomic pair correlation functions and their corresponding coordination numbers. The results of the interatomic distances for the *X*-O and O—O partial atomic pair correlation functions are presented in Table 2.

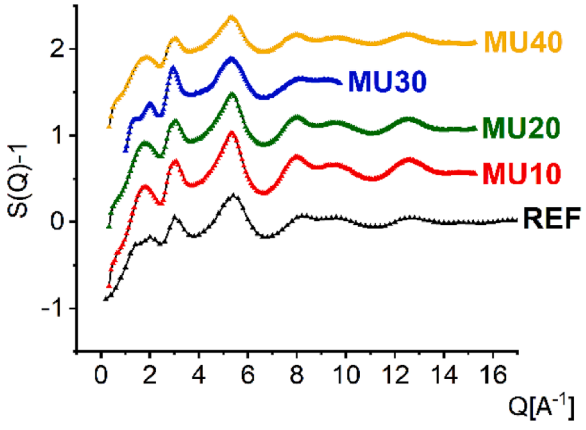

Fig. 1. Total ND structure factors for MU10 (red triangles), MU20 (green triangles), MU30 (blue triangles), and MU40 (yellow triangles) samples, along with RMC fits (black solid lines).

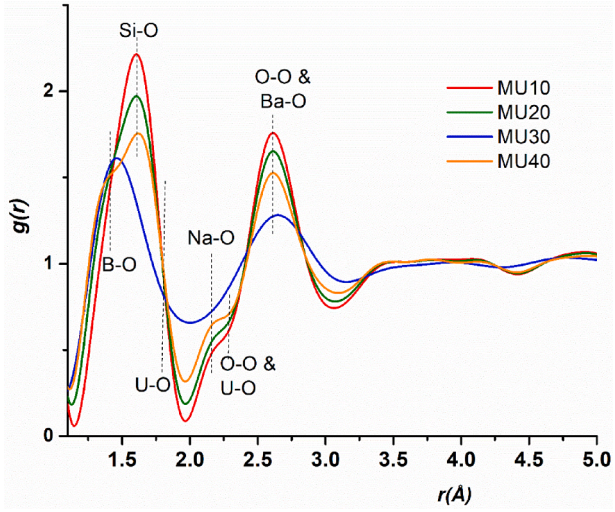

Fig. 2. Neutron pair distribution function, *g(r)* of borosilicate glasses containing 10, 20, 30 and 40 wt% of UO_3.

The partial pair correlation functions of Si-O, B-O, U-O and O—O atom pairs obtained by RMC analysis are shown in Fig. 3a, 3b, 3c and 3d respectively.

The length Si-O covalent bond (1.60±0.01 Å) did not change with the addition of UO_3 in the matrix glass. The observed Si-O interatomic distances are in excellent agreement with results reported in the literature [31-33]. Further the Si-O coordination values are 3.70±0.02, 3.86 ±0.05, 3.89±0.05, 3.90±0.05, and 3.70±0.1 for the REF, MU10, MU20, MU30, and MU40 samples, respectively and are given in Fig. 4 and Table 3.

The RMC results show that the Si-O network predominantly comprises of four-coordinated SiO_4 units, a characteristic consistently observed across the entire glass series. As a function of U concentration, there is a noticeable increase in the Si-O coordination number.

Table 2
Interatomic distances, r_{ij} [Å] obtained from the RMC simulation of neutron structure factors.

Samples	Si-O	B-O	Na-O	Ba-O	Zr-O	U-O	O-O
	Interatomic distance, r_{ij} [Å]						
REF	1.60 ± 0.01	1.40/ 1.60	2.10/ 2.65 ±0.02	2.60 ±0.03	2.00 ±0.02	–	2.30/ 2.60 ±0.03
		±0.02					
MU10	1.60 ± 0.01	1.35/ 1.60	2.14 ±0.02	2.70 ±0.03	2.00 ±0.02	1.75 ±0.02	2.45/ 2.69 ±0.03
		±0.02					
MU20	1.60 ± 0.01	1.30/ 1.60	2.15 ±0.02	2.70 ±0.03	2.00 ±0.02	1.79 ±0.02	2.44/ 2.68 ±0.03
		±0.02					
MU30	1.61 ± 0.01	1.50 ±0.02	2.12 ±0.02	2.68 ±0.03	2.04 ±0.02	1.80 ±0.02	2.52 ±0.03
MU40	1.60 ± 0.01	1.35/ 1.50	2.14 ±0.02	2.69 ±0.03	1.97 ±0.02	1.81 ±0.02	2.44/ 2.62 ±0.03
		±0.02					

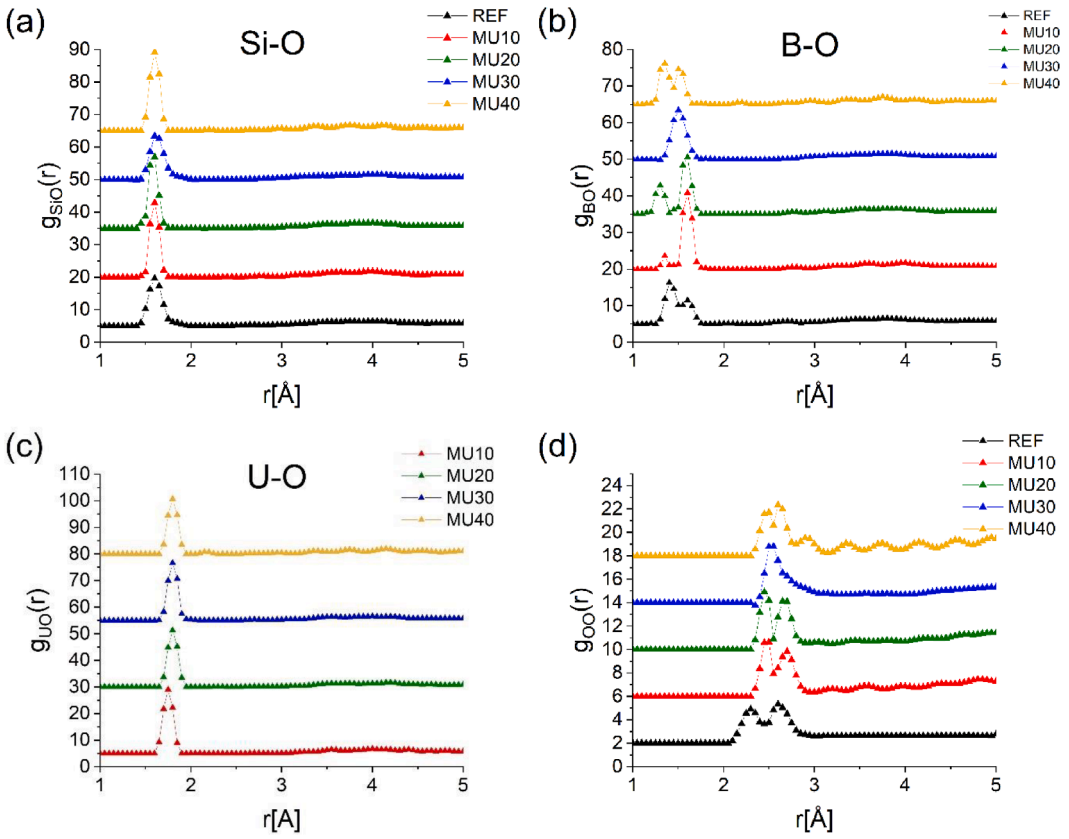

Fig. 3. Partial atomic pair correlation functions for Si-O (a), B-O (b), U-O (c) and O—O (d). Offset adjustments along the Y-axis have been used to enhance clarity.

Consequently, the number of non-bridging oxygen experiences a decrease, a trend observed up to 30 wt% UO_3 addition. However, in the case of the MU40 sample, a distinct decline in the Si-O coordination number is observed, which matches closely with value obtained for REF sample.

The B-O network shows show two well resolved peaks at 1.35/1.40±0.05 Å and at 1.60±0.02 Å, for MU10, MU20 and MU40, which are in agreement with the similar double peak distributions of REF sample, at 1.40 Å and 1.60±0.02 Å. The shorter distances are due to B-O bonds in trigonal units (BO_3), while the peak at 1.60 Å is due to borons in tetrahedral (BO_4) units. In case of MU30 sample, due to the lower *Q*-range of the neutron diffraction data, only one broad B-O distribution peak centered at 1.50±0.05 Å is found. The relative intensity of the two B-O peaks changes with the U concentration, the MU40 sample shows a notably greater intensity of the first peak at 1.35±0.05 Å, similar to the results for the REF sample. With a varying concentration of UO_3 in the glass, the relative area of the two B-O peaks undergoes modification [34]. The average B-O coordination number values shows a drastic enhancement from a value of 3.05 to 3.86 on adding 10 wt% of UO_3 in the base glass, however a further increase in UO_3 concentration from 20 to 40 wt% steadily decreases B-O coordination to 3.64±0.05, 3.45±0.05 and 3.24±0.08 for samples MU20, MU30 and MU40, respectively, as shown in Table 3. A similar tendency is observed for the alkali borosilicate glasses reported in the literature [35], from which it can be concluded that UO_3 plays a role of an intermediate oxide. Based on literature, under the incorporation of lanthanides and alkali metals, there is an observed increase in the B-O coordination number within borosilicate glasses. These metal-oxides actively modify the glass structure, resulting in a reduction of non-bridging oxygen. On the contrary, the introduction of large amounts of U disrupts the borate network, leading to a decrease in the coordination number and an increase in the number of non-bridging oxygens [34-36].

The partial atomic pair correlation functions were determined for the U-O atomic pair as well, revealing a characteristic distance at 1.80±0.03 Å. A slightly shorter distance of 1.75±0.02 Å was observed for the MU10 sample as shown in Fig. 3.

Within borosilicate glasses, the U coordination environment typically comprises two types of oxygen species. Conventionally, two O atoms occupy axial positions around the U, with a characteristic distance of approximately 1.80 Å. Depending on the specific glass composition or the conditions of melt quenching, an additional 3 to 5 O atoms assume equatorial positions around U, characterized at longer distances as stated in literature [37-39]. This facilitates the formation of UO_6 clusters within the local structure, characterized by a fixed combination of uranium coordination numbers in both the pentavalent U^V and hexavalent U^{VI} states.

The O—O partial atomic pair correlation function reveals two distinct peaks, the interatomic distances can be found in Table 2. The first peak is observed at 2.45±0.03 Å, and the subsequent peak appears at around 2.65±0.03 Å [40,41]. However, for the MU30 sample, a single peak is evident, positioned at 2.52±0.03 Å. There is no visible dependence on U-concentration for the Na-O, Ba-O, and Zr-O functions; typically, the position of each peak remains consistent. Specifically, the Na-O peaks can be found at around 2.15±0.02 Å [42,43], the Ba-O peaks at around 2.70±0.03 Å [44,45], and the Zr-O peak is approximately at 2.00±0.02 Å, which is a slightly shorter as reported in literature [46,47].

From the RMC simulation several second neighbor partial atomic pair correlation functions have been obtained. The results for Si-B, Si-U and B-U second neighbor partial atomic pair correlations are displayed in Fig. 5. The Si-B correlation observed at 2.70±0.1 Å, 2.70±0.1 Å, 2.70 ±0.1 Å, 2.75±0.1 Å, and 2.65±0.1 Å for the REF, MU10, MU20, MU30, and MU40 samples, respectively, which indicates potential linkages between Si-and B-centered groups [40,48]. The medium-range structural order within the glass system is attributed to the interconnection of SiO_4 and BO_3/BO_4 units. A significant correlation is evident among the tetrahedral SiO_4, trigonal BO_3, and tetrahedral BO_4 structural units. By

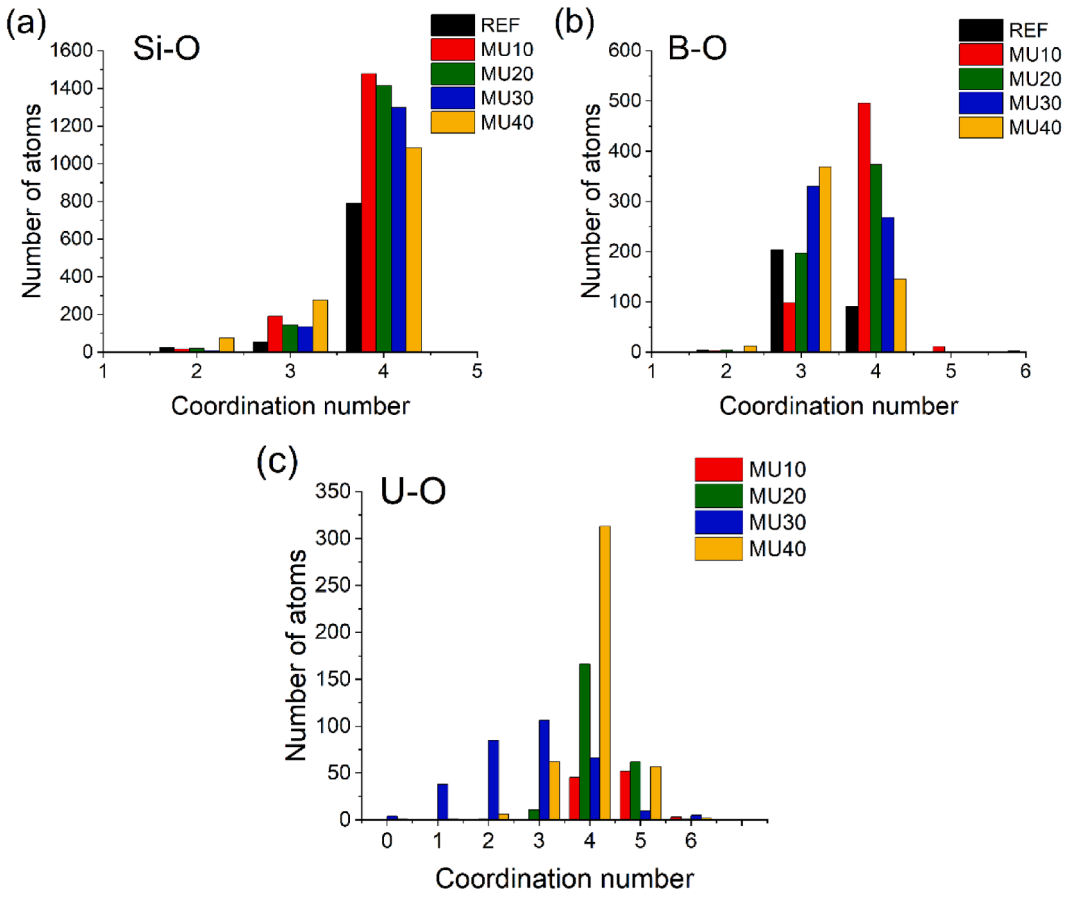

Fig. 4. Si-O (a), B-O (b) and U-O (c) coordination number distribution calculated by RMC modeling for the glass samples.

Table 3
The average coordination number denoted as CN_{ij}. The interval provided in brackets signifies the range within which the RMC simulation was calculated.

Atom pairs	REF	MU10	MU20	MU30	MU40
	Coordination number, CN_{ij}				
Si-O (r_1:–1.45–- r_2: 2.00)	3.70 ±0.02	3.86 ±0.05	3.89 ±0.05	3.90 ±0.05	3.70 ±0.1
B-O (r_1:–1.00–- r_2: 1.85)	3.05 ±0.02	3.86 ±0.03	3.64 ±0.05	3.45 ±0.05	3.24 ±0.08
U-O (r_1–1.6–- r_2: 2.70)	—	4.58 ±0.05	4.21 ±0.05	5.0 ± 0.05	3.95 ±0.06

using RMC calculations, we clarify the fundamental network structure, revealing a composition that includes mixed ^{IV}Si-O-^{III}B and ^{IV}Si-O-^{IV}B linkages [48,49], as concentrations increase, ^{IV}Si-O-^{III}B linkages progressively take on a more dominant role. Our findings reveal that the studied glass compositions establish a stable system characterized by these units, similar to the matrix glass, even in the case of the MU40 sample.

U typically forms bonds with non-bridging oxygen atoms in axial positions, which exhibit no active linkage to other atoms such as B or Si. In contrast, oxygen atoms occupying the equatorial position establish connections with B atoms, leading to the formation of BO_3 triangles [27]. This phenomenon reveals the reduction in the coordination number of boron from 4 to 3, which is also supported by the changes of the B-O peak positions. The second neighbor distances for Si-U and B-U pairs (Table 4), dominantly appear at 3.15±0.1 Å, which are generally shorter than those reported in literature [27]. The results suggest that U atoms form connections through an oxygen atom with the network former, actively contributing to the establishment of the stable network structure.

3.2. *Oxidation state of uranium by XANES and uranium environments by EAXFS*

Uranium was added in the glass matrix system in the form of UO_3 as U^{VI}. The results of ND suggest that uranium predominantly exists in the states of U^{VI} and U^{V} within the sample series, however, it can be further reduced to U^{IV} and may occur in an 8-fold coordination. During the evaluation of the results, consideration was given to the potential occurrence of uranium in this reduced state, specifically U^{IV} within our system. The normalized XANES spectra and the first derivatives of the normalized spectra collected in transmission mode are presented in Fig. 6a, which also includes the spectra for reference compounds: UO_2, U_3O_8 and UO_3.

The standards were used to investigate the oxidation state. However, it must be taken into account that the reference compound – U_3O_8 – contains uranium not entirely in the form of U^{V}, but as 1/3 of U^{VI} and 2/3 of U^{V}, as can be represented by $U^{VI}U^{V}_2O_8$. The U L_{III}-edge shows a consistent shape and position across all the samples. Fig. 6 shows the positions of the edge energy of the glassy specimens, which remains unchanged despite the increasing uranium loading, the exact positions are presented in Table 5.

Based on the results, the oxidation state of uranium does not change within the series. Considering the edge energy positions, the samples show a mixed oxidation states, both U^{VI} and U^{V} appear in the sample, however the presence of U^{IV} cannot be ruled out. Linear combination fitting (LCF) was used to further confirm our results, during the analysis consideration was given to the potential occurrence of uranium in the reduced U^{IV} state, however, in all instances, a degradation of the fit was observed, prompting subsequent fittings to be exclusively performed

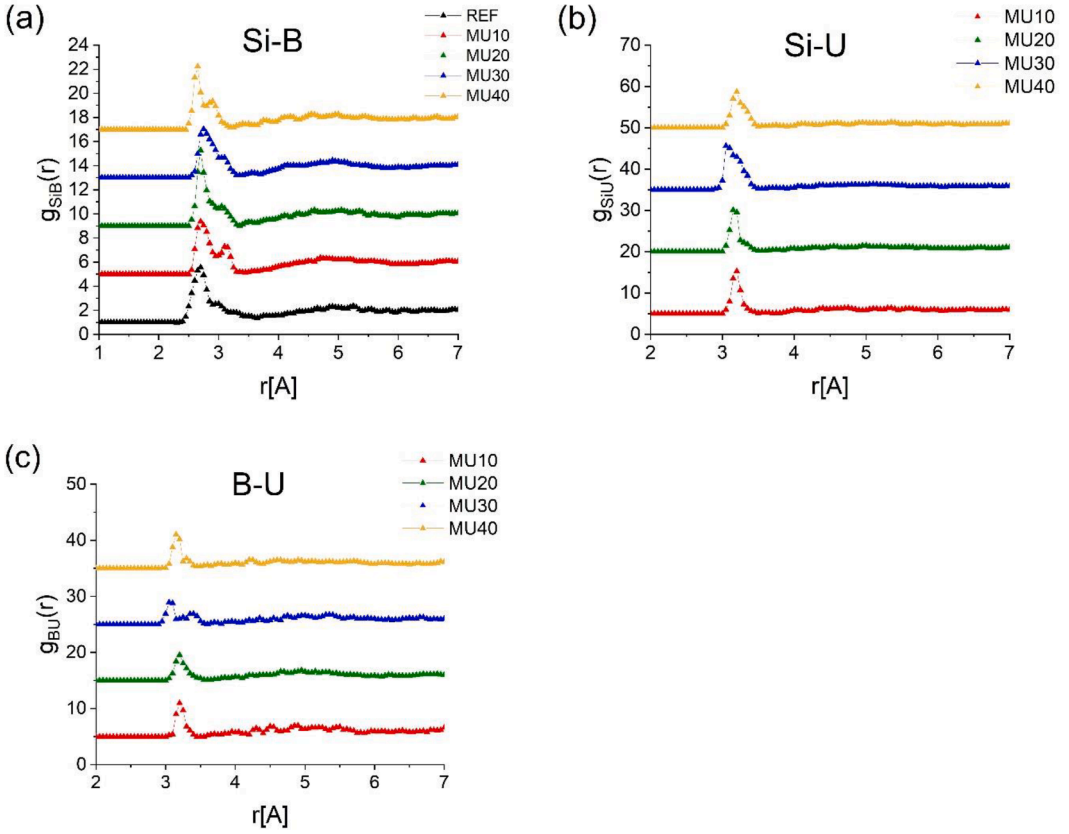

Fig. 5. Si-B (a), Si-U (b) and B-U (c) atomic pair correlation functions obtained by RMC technique. Offset adjustments along the Y-axis have been used to further enhance readability.

Table 4
Interatomic distances, r_{ij} [Å] obtained from the RMC simulation for the Si-B, Si-U and B-U atom pairs (second neighbor distances).

Atom pairs	REF	MU10	MU20	MU30	MU40
	Interatomic distance, r_{ij} [Å]				
Si-B	2.70±0.1	2.70±0.1	2.70±0.1	2.75±0.1	2.65±0.1
Si-U	–	3.20±0.1	3.18±0.1	3.07±0.1	3.2 ± 0.1
B-U	–	3.20±0.1	3.20±0.1	3.05±0.1	3.15±0.1

with the spectra of the UO_3 and U_3O_8 reference compounds. The LCF results show that the samples contain both hexavalent and pentavalent uranium, their ratios are found to be very similar within the series. Similar oxidation states can be observed in literature [50], where 8.48 to 28.29 wt% UO_3 was also loaded in sodium borosilicate glass. Our results obtained for the hexavalent form are lower compared to the result obtained in literature [51], where with 5.3 wt% U_3O_8 loading about 80 % in the hexavalent form.

The normalized EXAFS spectra were analyzed to investigate the local environment, the fitting for the four samples performed simultaneously. The Fourier transforms (FT) for the studied glass species are shown in Fig. 7 and the best fit parameters such as interatomic bond distance and Debye-Waller factor (σ^2) are shown in Table 6.

Based on the XANES results different models were used for fitting to find the most adequate model. As for the best fit, U^{VI} is present as uranyl, i.e. linear arrangement with 2 O atoms ($O = U = O$) and 6 O atoms in an equatorial plane, and U^{V} in octahedral coordination. The best fit was achieved using this model, the results are in agreement with XANES as well.

Hexavalent uranium exists in the form of UO_2^{2+}, where two different U-O distances can be observed, where the white line lies closer to the respective in UO_3. The two nearest linear oxygen in the axial position are located at 1.83±0.01 Å, 1.83±0.01 Å, 1.85±0.01 Å and 1.84±0.01 Å for MU10, MU20, MU30 and MU40, whereas the 6 equatorial oxygen atoms are located at longer distance of 2.27±0.03 Å, 2.27±0.03 Å, 2.27±0.03 Å and 2.26±0.03 Å for MU10, MU20, MU30 and MU40, respectively. These results are not influenced by the different composition of the glassy samples and comparable with the results obtained in literature [38,50,51].

3.3. Thermal characteristics of the glasses

Based on the heat flow and relative mass change rate (DTG) curves, as shown in Fig. 8 and Table 7, the base REF glass shows very high stability up to 1300°C.

The DTG curve of the REF sample is in good coincidence with the zero background and starts to show continuously increasing mass loss only above ca. 1200 °C. Heat flow curve of the REF base glass exhibits shifts toward negative values, which indicates the appearance of a glass transition events at about T_g=649±1 °C (the T_g values were determined from the inflection points). Additional shifts in the thermal curve above this temperature up to 1200 °C may be identified as small exothermic events (with 785 °C and 930 °C). Regarding the U-loaded glass samples, the T_g value increased in all cases and are well above the detectable T_g value of the REF sample. The obtained values are 725 °C, 700 °C, 716 °C and 711 °C for the MU10, MU20, MU30 and MU40 samples, respectively (Fig. 9).

Similarly, increased T_g values compared to that of matrix glass due to the addition of UO_3 is reported in the literature [52]. The phenomenon can be explained by the formation of strong U-O clusters, which is also contributed to by the fact that the substituent ions play the role of network formers instead of network modifiers.

On contrary to the change of the stability between the REF and U containing samples, all the MU10-MU40 samples exhibit weight loss in a

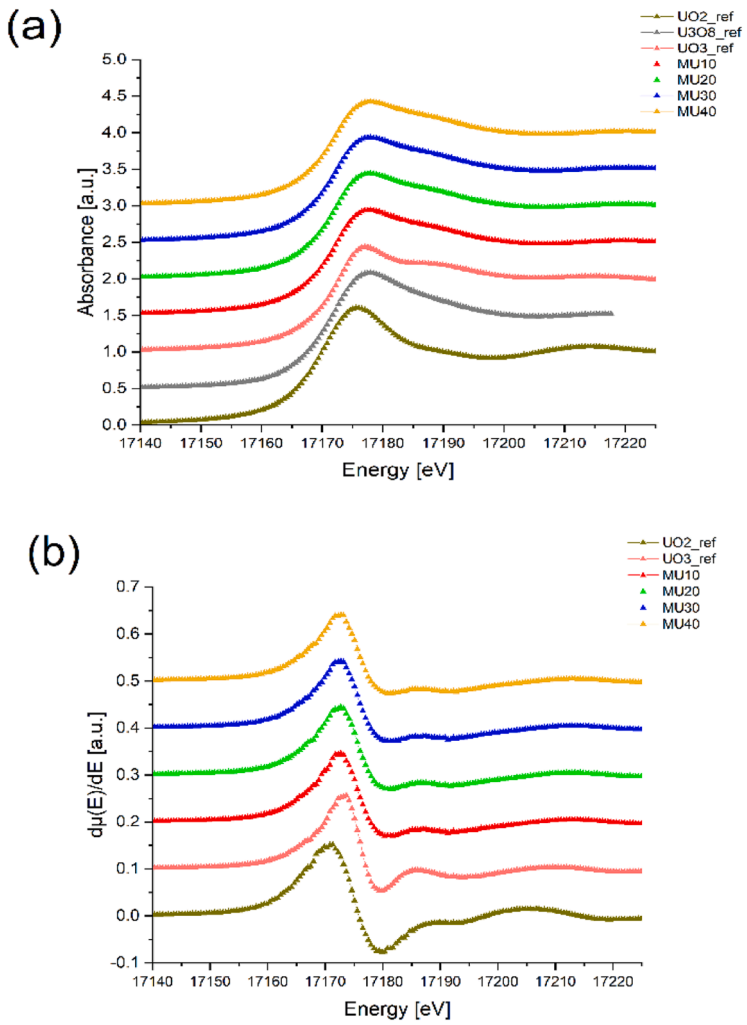

Fig. 6. Normalized XANES spectra (a) and their first derivates (b) collected in transmission mode for the U-loaded samples and reference compounds.

Table 5
U L_{III}-edge energy positions of the references and the studied glassy systems.

Samples	Edge position [eV]
UO_2	17,171.3
U_3O_8	17,172.5
UO_3	17,173.6
MU10	17,172.7
MU20	17,172.8
MU30	17,172.7
MU40	17,172.8

wide temperature range between room temperature and about 700 °C. In this range the DTG have a sharp weight loss peak at about 100 °C and a broader peak between 500 and 700 °C. Parallel to the DTG signal, the heat flow curves show also smaller changes around the zero heat flow background.

Regarding stability, the MU30 glass is the most similar to the REF basic composition. To characterize this stability, the weight loss differences were determined for three regimes, i.e. for up to 700 °C (DTRT-700), between 700 and 1300 °C (DT700–1300) and 1300–1500 °C (DT1300–1500) for all compositions. Table 7 shows these characteristic weight loss values (the values are the negative integral of the DTG curves between the indicated limits).

As seen from Table 7, the DT values of MU30 are comparable to that of REF and are significantly smaller than the other glass compositions.

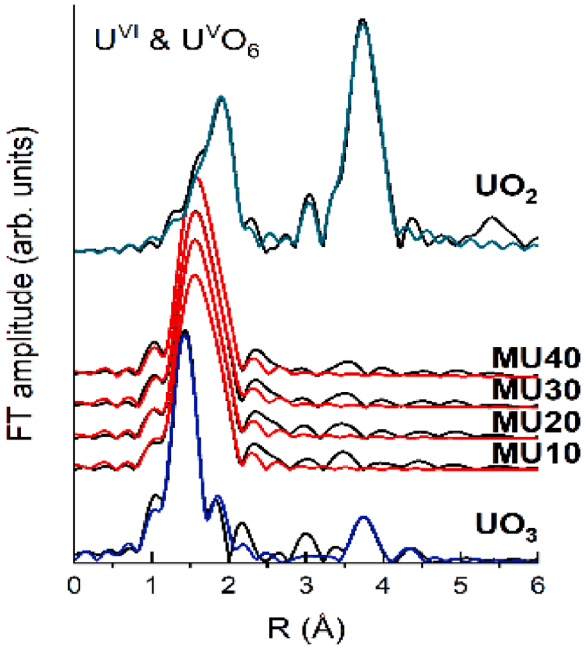

Fig. 7. The Fourier transform of the EXAFS spectra for the glassy specimens.

Table 6
Structural parameters obtained for the U-loaded glassy specimens using the best EXAFS fitting model via analyzing the U-L_{III} edge of the EXAFS spectra. (The results marked in italic style present U^{V} in octahedral coordination.).

		U^{VI} [%]	R [Å]	σ^2 [$\times 10^{-3}$ Å^2]	R [Å]	σ^2 [$\times 10^{-3}$ Å^2]
FIT-A	**MU10**	63 ± 4	1.86 ±0.01	2.7	1.83 ±0.02	6.1
			2.25 ±0.03	5.2		
	MU20	62 ± 7	1.85 ±0.01	1.5	1.83 ±0.02	11.4
			2.25 ±0.03	4.8		
	MU30	66 ± 3	1.85 ±0.01	1.6	1.81 ±0.02	11.2
			2.25 ±0.03	2.4		
	MU40	64 ± 3	1.85 ±0.01	1.7	1.82 ±0.02	12.6
			2.26 ±0.03	4.8		

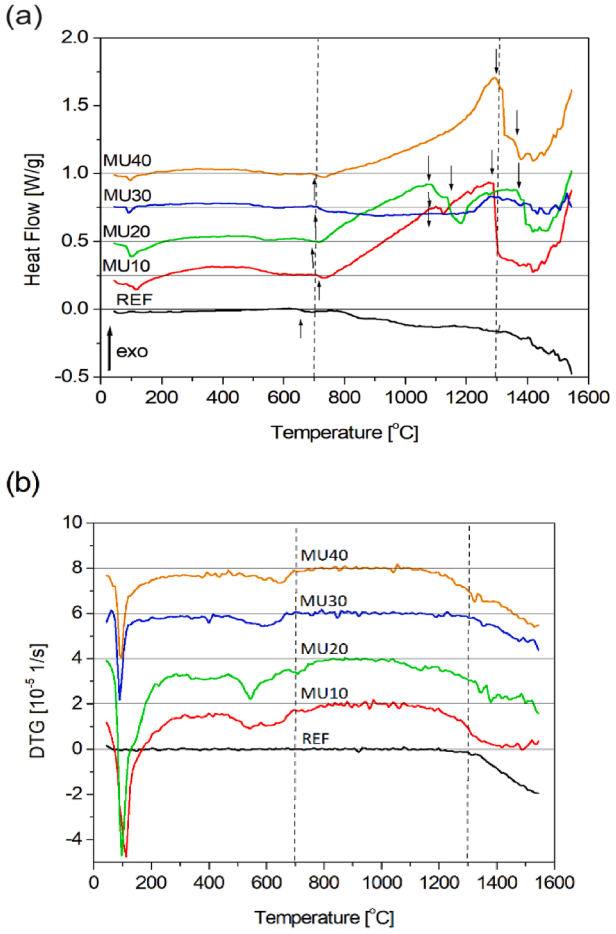

Fig. 8. Heat flow (a) and relative mass change rate (DTG) curves (b) for REF and MU10-MU40 samples.

Practically the same order of stability (REF > MU30 > MU40 > MU10 > MU20) can be determined from both DTRT-700 and DT700–1300. In agreement with the DT values, MU10, MU20 and MU40 exhibit gradually increasing strong exothermic signal above 700 °C. These signal components with the corresponding zero DTG signal indicate the presence of devitrification processes in these glasses between approximately 700 and 1200 °C. Similar behavior can be observed even in the MU30 sample at 1200 °C but much smaller extent. The devitrification processes are terminated with drops of the exothermic signal. These drops probably indicate partial melting of the crystallized glass as these features are much weaker in the supercooled liquids of the REF and MU30 higher stability glasses.

Table 7
Thermal characteristics of the different glasses, where $DT_{RT\text{-}700}$ $DT_{700–1300}$ and $DT_{1301.70–1500}$ are relative weight losses between the indicated temperatures, T_g is glass transition temperature and T_{on} is the onset temperature of a drop in the exothermic signal.

Samples	$DT_{RT\text{-}700}$ [10^{-4}]	$DT_{700–1300}$ [10^{-4}]	$DT_{1300–1500}$ [10^{-4}]	T_g [°C]	T_{on} [°C]
REF	0	3.6	103.4	649	–
MU10	489.2	66.8	204.6	725	1086, 1289
MU20	579.4	100.4	182.8	700	1081, 1137, 1368
MU30	144.7	4.9	81.7	716	1285
MU40	227.3	49.8	194.9	711	1300, 1363

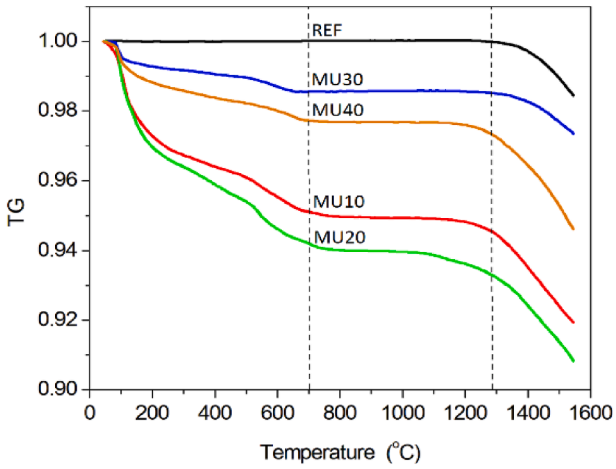

Fig. 9. Relative mass change (TG) curves for REF and MU10-MU40 samples.

3.4. Leachate solution analysis

The ICP-OES results of the leachates and the initial porewater are shown in Table 8.

Compared to the initial porewater, elevated concentrations of Si, B,

Table 8
ICP-OES results of the liquid phases of the REF, MU10, MU20, MU30 and MU40 sample leachates and the initial porewater.

Samples	Si [mg/l]	B	Na	Ba	Zr	U
SBPW	5.9	0.12	492	–	–	–
REF – 3D	152	44.5	780	0.501	<LOD	–
MU20 – 3D	1240	92.6	1560	0.402	<LOD	0.317
MU30 – 3D	34.5	19.0	478	0.521	<LOD	0.202
MU40 – 3D	166	17.8	649	0.469	<LOD	0.030
REF – 7D	335	76.9	993	0.587	<LOD	–
MU20 – 7D	2390	170	2230	0.609	<LOD	0.631
MU30 – 7D	60.3	25.5	533	0.264	<LOD	0.147
MU40 – 7D	54.6	6.4	680	0.492	<LOD	0.386
REF – 10D	397	82.3	1120	0.556	<LOD	–
MU10 – 10D	2700	290	2400	1.38	<LOD	0.205
MU20 – 10D	3100	228	2560	1.34	<LOD	1.225
MU30 – 10D	62.5	25.9	547	0.272	<LOD	0.124
MU40 – 10D	443	42.3	913	0.268	<LOD	0.418

Table 9
contains the normalized concentration, the normalized mass loss and glass solution rates calculated for Si, B and U.Table 9 Normalized concentration, normalized mass loss and glass dissolution rate measured in PCT-B test from 3 to 10 days for silicon, boron and uranium of the U-loaded sample series.

	REF 3D	MU20 3D	MU30 3D	MU40 3D	REF 7D	MU20 7D	MU30 7D	MU40 7D	REF 10D	MU10 10D	MU20 10D	MU30 10D	MU40 10D
***NC*(Si) [g/l]**	0.686	7.003	0.222	1.247	1.516	13.42	0.388	0.410	1.787	13.52	17.42	0.402	3.319
***f*(Si) -**	0.222	0.178	0.156	0.133	0.222	0.178	0.156	0.133	0.222	0.200	0.178	0.156	0.133
***NL*(Si) [g/m^2]**	0.43	4.37	0.14	0.78	0.94	8.37	0.24	0.25	1.11	8.46	10.86	0.25	2.07
d_{eq}(Si) [µm]	0.09	0.78	0.02	0.13	0.21	1.49	0.04	0.04	0.25	0.73	1.94	0.04	0.34
***NR*(Si) [g/(m^{2}d)]**	0.142	1.455	0.046	0.260	0.134	1.195	0.035	0.036	0.111	0.846	1.086	0.025	0.207
***NC*(B) [g/l]**	1.400	3.647	0.853	0.933	2.424	6.699	1.147	0.337	2.592	10.161	8.987	1.169	2.221
***f*(B) -**	0.032	0.025	0.022	0.019	0.032	0.025	0.022	0.019	0.032	0.029	0.025	0.022	0.019
***NL*(B) [g/m^2]**	0.87	2.27	0.53	0.58	1.50	4.18	0.72	0.21	1.61	6.36	5.60	0.73	1.39
d_{eq}(B) [µm]	0.19	0.41	0.09	0.10	0.33	0.74	0.12	0.04	0.36	0.55	1.00	0.12	0.23
***NR*(B) [g/(m^{2}d)]**	0.290	0.758	0.178	0.194	0.214	0.597	0.102	0.030	0.161	0.636	0.560	0.073	0.139
***NC*(U) [g/l]**	–	0.002	0.001	8.96E-05	–	0.004	0.001	0.001	–	0.002	0.007	4.99E-04	0.001
***f*(U) -**	–	0.166	0.249	0.332	–	0.166	0.249	0.332	–	0.083	0.166	0.249	0.332
***NL*(U) [g/m^2]**	–	1.19E-03	5.07E-04	5.60E-05	–	2.37E-03	3.69E-04	7.23E-04	–	1.54E-03	4.60E-03	3.12E-04	7.86E-04
d_{eq}(U) [µm]	–	0.06	0.02	0.002	–	0.11	0.02	0.03	–	0.04	0.22	0.01	0.03
***NR*(U) [g/(m^{2}d)]**	–	3.97E-04	1.69E-04	1.87E-05	–	3.38E-04	5.27E-05	1.03E-04	–	1.54E-04	4.60E-04	3.12E-05	7.86E-05

and Na can be observed in the leachates, the measured higher concentrations can be traced back to glass dissolution. As time progresses, an increasing trend in the concentrations can be observed in the REF sample series, providing a useful point of comparison for assessing the U-loaded samples. Notable differences can be observed in the concentrations of samples containing 10–20 wt% and 30–40 wt% uranium. For samples with lower UO_3 content, the concentrations of the elements of interest in the leachates are higher than those in the REF sample, however, starting from a 30 wt% UO_3, lower values were measured compared to the REF series. The concentrations of Si and B are consistently one or even two orders of magnitude higher in samples with lower UO_3 content (10–20 wt%), while the values for Ba and U measured only after 10 days are one order of magnitude higher. Si, B and Na follow a similar tendency during the leaching experiment, in the sample series containing 20 and 30 wt% uranium, the concentrations increase as the days progress, only in the MU40 series is a unique phenomenon observed for Si and B elements, where on the seventh day the concentration decreases, then increases again on the tenth day. Ba can be characterized by an increasing concentration in the case of sample MU20, the tenth day results of MU10 and MU20 are very similar, so it can be assumed that they share a similar trend, on contrary, in the case of samples MU30 and MU40, the initial Ba concentration by the end of the corrosion test is almost halved. U shows an increasing trend for all sample series, except for sample MU30, where the amount of leached Uranium decreases as time progresses. Zirconium was below the detection limit in all cases.

The *NC* value of U is lower than that measured for the major constituent elements of the glass as shown in literature [53], values typically 3–5 orders of magnitude lower were calculated in the case of our sample series. Due to its high solubility, B most effectively shows the extent of glass dissolution. In the case of B, the glass dissolution rate shows a decreasing trend for the MU20 and MU30, while in the case of MU40 the decrease can be found on the seventh day in the same way as in the concentrations measured by ICP-OES. The average glass dissolution rate mainly occurred in hundredths order of magnitude, an order of magnitude lower value can be measured in the case of MU30–10D and MU40–7D. A similar trend characterizes the dissolution rate of Si and U, which suggests that dissolution is hindered by the formation of a surface layer that prevents further glass loss [10,54]. The dissolution rate of the MU30 sample is the lowest among the U-loaded samples, with values even lower than those of the REF sample, and the dissolution rate for U is also the lowest for the MU30 sample series compared to the other samples containing UO_3.

Based on the decreasing tendency and low final values on the tenth day, the MU30 sample tends to be most stable at the leaching test conditions, therefore, in the case of the MU30 sample an extended leaching test was carried out for 180 days with MQ-water as the leaching solution for a standard PCT at neutral pH. The normalized concentration, normalized mass loss and glass dissolution rates are presented in Table 10.

The results of the leaching tests conducted with SBPW exhibit increased corrosiveness compared to MQ-water at a neutral pH. The alkaline nature of the porewater and significantly higher salt levels contribute to increased normalized mass loss, most noticeable in the case of Si and U, where the values are two orders of magnitude higher in the case of Si, and one order of magnitude higher in the case of U. Despite the different leaching solution, the B normalized mass loss is very similar, the magnitude difference is visible only on the 10th day, where it is 0.161 g/(m^{2}d) in the case of SBPW, and 0.073 g/(m^{2}d) in the case of MQ-water. During our previous work, a PCT-B protocol was performed according to ASTM on the REF glass sample [25], comparing

Table 10
Extended PCT test on the glass sample containing 30 wt% UO_3 in MQ-water medium at neutral pH.

	MU30 3D	MU30 7D	MU30 10D	MU30 30D	MU30 90D	MU30 180D
***NC*(Si) [g/l]**	6.30	11.58	15.83	31.70	47.50	52.50
***f*(Si) -**	0.156	0.156	0.156	0.156	0.156	0.156
***NL*(Si) [g/m^2]**	4.06	7.45	10.22	20.40	30.56	33.66
d_{eq}(Si) [µm]	0.68	1.24	1.70	3.40	5.10	0.56
NR(Si) [g/(m^{2}d)]	1.35	1.06	1.02	0.68	0.34	0.19
NC(B) [g/l]	1.02	1.88	2.51	5.15	7.34	8.46
f(B) -	0.022	0.022	0.022	0.022	0.022	0.022
NL(B) [g/m^2]	0.66	1.21	1.61	3.31	4.72	5.37
d_{eq}(B) [µm]	0.11	0.20	0.27	0.55	0.79	0.09
***NR*(B) [g/(m^{2}d)]**	0.219	0.173	0.161	0.110	0.052	0.030
***NC*(U) [g/l]**	7.50E-03	7.12E-03	8.09E-03	2.01E-02	4.26E-02	8.43E-02
***f*(U)**	0.249	0.249	0.249	0.249	0.249	0.249
***NL*(U) [g/m^2]**	4.83E-03	4.58E-03	5.19E-03	1.30E-02	2.74E-02	5.41E-02
d_{eq}(U) [µm]	0.001	0.001	0.001	0.002	0.005	0.001
***NR*(U) [g/(m^{2}d)]**	1.61E-03	6.54E-04	5.19E-04	4.32E-04	3.04E-04	3.00E-04

the two samples, no significant differences can be observed. As time progresses, the concentration of each element decreases and reaches saturation. Based on the data, it was confirmed that U incorporated into the glass structure, acting as a glass former and enhancing leaching resistance. As time progresses, the amount of uranium entering the leaching solution decreases and the mass loss slows down [10].

3.5. Hardness of the MU30 and REF samples

As the MU30 sample showed the most promising results based on the thermal and leaching analysis, its hardness was measured and compared with that of the REF sample. The measured *EIT* and *HIT* values are presented in Table 11 alongside with the hardness in the traditional "Vickers" unit and the number of repetitions.

The modulus for the REF sample is 77.4 ± 1.3 GPa, while the MU30 sample has a modulus of 71.6 ± 0.7 GPa. The results are comparable with data reported on other borosilicate glasses reported in the literature [55]. The modulus of the different borosilicate glasses was around 75 GPa, the changes in the microstructure are primarily not influenced by the composition, but by the *R* value, which refers to the ratio of Na_2O and B_2O_3. The *R* value of both REF and MU30 samples was 2.5, therefore the difference in modulus and hardness was only influenced by 30 wt% UO_3 loading.

As can be seen from the nanoindentation load-depth curve in Fig. 10 from the deeper indentation depth, and from the lower hardness values, (6650±160 MPa compared to 7390±140 MPa) the microstructure of the U loaded MU30 sample is ~ 11 % weaker than that of the REF sample.

4. Conclusion

Borosilicate glass matrix ($55SiO_2{\cdot}10B_2O_3{\cdot}25Na_2O{\cdot}5BaO{\cdot}5ZrO_2$) loaded with 10, 20, 30 and 40 wt% UO_3 were studied by neutron diffraction in combination with RMC and X-ray absorption techniques (XANES, EXAFS) in order to elucidate the effects of uranium on the borosilicate glass short-range structural properties, such as B-O, Si-O, Na-O, U-O and O—O distances and coordination environment. DTA, leaching and nanoindentation studies were also carried out to investigate the chemical and thermal stability and mechanical properties of the glasses.

Neutron diffraction revealed that with the incorporation of uranium with an increasing concentration, no significant changes occur in the basic silicate network compared to the REF sample and loading of up to 40 % % wt of UO_3 produces completely glassy phase by melt quenching process. By using RMC calculations, the fundamental network structure was found to be made of mixed ^{IV}Si-O-^{III}B and ^{IV}Si-O-^{IV}B linkages. On increasing uranium concentration ^{IV}Si-O-^{III}B linkages progressively take on a more dominant role. U typically forms bonds with non-bridging oxygen atoms in axial positions, which exhibit no active linkage to other atoms such as B or Si. This phenomenon reveals the reduction in the coordination number of B from 4 to 3. The best EXAFS fit confirmed that U^{VI} ions are present as uranyl, i.e. linear arrangement with 2 O atoms ($O = U = O$) and 6 O atoms in an equatorial plane, and U^{V} in octahedral coordination and their ratios are found to be very similar within the series.

The REF borosilicate glass shows very high thermal stability up to 1300 °C and among U loaded glasses, the MU30 sample has the best thermal stability, although thermal stability is found to deteriorate significantly with U incorporation in the glass matrix. Based on the leaching studies, a notable difference can be observed in the concentrations of samples containing 10–20 wt% and 30–40 wt% UO_3. For samples with lower UO_3 content, the concentrations in the leachates are higher than those in the REF sample, however, starting from a 30 wt% UO_3, lower values were measured compared to the REF series. The dissolution rate of the MU30 sample is the lowest among the U-loaded samples, with values even lower than those of the REF sample, and the dissolution rate for U is also the lowest for the MU30 sample series compared to the other samples containing UO_3.

Mechanical properties of the REF and MU30 samples were investigated with nanoindentation. The modulus for the REF sample is 77.4 ± 1.3 GPa, while the MU30 sample has a modulus of 71.6 ± 0.7 GPa. The deeper indentation depth and the lower hardness values (6650±160 MPa compared to 7390±140 MPa) indicate that the microstructure of the MU30 sample is ~ 11 % weaker than that of the REF sample. Consequently, it is concluded that the studied borosilicate glass matrix can accommodate UO_3 up to at least 40 wt%, indicating significant potential for its application in high-level nuclear waste management.

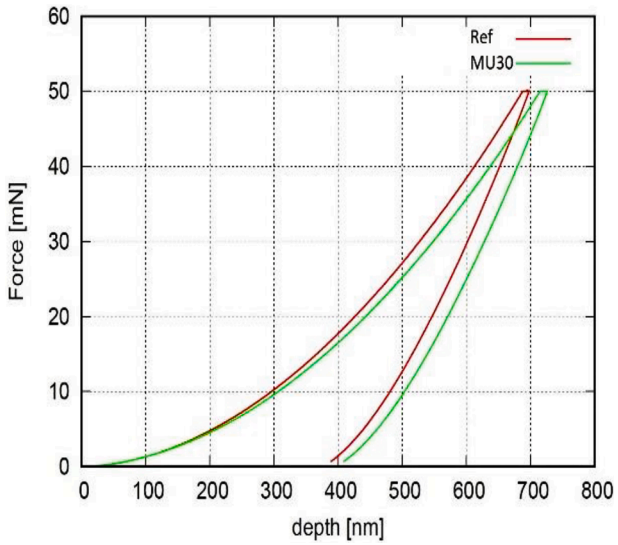

Fig. 10. Nanoindentation load-depth curve for REF and MU30 samples.

Table 11
EIT and HIT values of REF and MU30 samples alongside with hardness in the traditional "Vickers" unit and the number of repetitions.

	EIT [GPa]	*HIT* [MPa]	*HVIT* [Vickers]	N [-]
REF	77.4	7390	697	19
Std dev.	1.3	140	14	–
MU30	71.6	6650	628	17
Std dev.	0.7	160	15	–

Ethical approval

Not applicable.

CRediT authorship contribution statement

I. Tolnai: Investigation, Formal analysis, Writing – original draft. **J. Osan:** Investigation, Data curation, Formal analysis, Writing – review & editing. **F. Pinakidou:** Formal analysis. **Zs. Kovacs:** Investigation, Formal analysis. **M. Fabian:** Conceptualization, Methodology, Investigation, Resources, Writing – review & editing.

Declaration of competing interest

The authors declare the following financial interests/personal relationships which may be considered as potential competing interests: Margit Fabian reports financial support was provided by EU Framework Programme for Research and Innovation Euratom. If there are other authors, they declare that they have no known competing financial interests or personal relationships that could have appeared to influence the work reported in this paper.

Data availability

Data will be made available on request.

Acknowledgements

The research was partly supported by the European Union's Horizon 2020 research and innovation program through the EURATOM project European Joint Programme on Radioactive Waste Management (EURAD) Assessment of chemical evolution of Intermediate Level Waste and High Level Waste disposal cell (ACED) work package (EU grant agreement number: 847593). One of the authors (M.F.) acknowledge that this project was party supported by the János Bolyai Research Scholarship of the Hungarian Academy of Sciences. The authors would like to thank Diamond Light Source for beamtime (proposal SP33573), and the staff of beamlines B18 for assistance with measurements and data collection. The authors are grateful to Tamas Kolonits who performed the nanoindentation measurements. Two anonymous reviewers are also greatly acknowledged for their detailed and relevant comments.

Supplementary materials

Supplementary material associated with this article can be found, in the online version, at doi:10.1016/j.jnoncrysol.2024.123054.

References

[1] M. Ojovan, W. Lee, An Introduction to Nuclear Waste Immobilisation, 17, Elsevier Ltd, 2014, pp. 245–282. ISBN:978-0-08-099392-8 Chapter.
[2] W.E. Lee, M.I. Ojovan, M.C. Stennett, N.C. Hyatt, Immobilisation of radioactive waste in glasses, glass composite materials and ceramics, Adv. Appl. Ceramics 105 (1) (2006) 3–12, https://doi.org/10.1179/174367606x81669.
[3] M.I. Ojovan, W.E. Lee, Glassy wasteforms for nuclear waste immobilization, Metall. Mater. Trans. a Phys. Metall. Mater. Sci. 42 (2011) 837–851, https://doi.org/10.1007/s11661-010-0525-7.
[4] D. Barbatova, V. Necas, Multi-barrier system model of the geological repository for spent nuclear fuel, Nuclear 2016 (2016) 6–12.
[5] Organisation for Economic Co-operation and Development and Nuclear Energy Agency, Engineered barrier systems and the safety of deep geological repositories: state-of-the-art report, OECD Publishing, 2003, pp. 9–11.
[6] L. Rodríguez-Penalonga, B. Yolanda Moratilla Soria, A review of the nuclear fuel cycle strategies and the spent nuclear fuel management technologies, Energies. 10 (8) (2017) 1235, https://doi.org/10.3390/en10081235.
[7] C.M. Jantzen, M.I. Ojovan, On selection of matrix (Wasteform) material for higher activity nuclear waste immobilization (Review), Russian J. Inorganic Chem. 64 (2019) 1611–1624, https://doi.org/10.1134/S0036023619130047.
[8] E. Bitay, I. Kacsó, E. Veress, Chemical durability of uranium oxide containing glasses, Acta Materialia Transilvanica 1 (2019) 12–18, https://doi.org/10.2478/amt-2018-0004.
[9] J.L. George, T. Sugawara, T. Ohira, A.A. Kruger, J.D. Vienna, Heat capacity of complex aluminoborosilicate glasses, Int. J. Appl. Glass. Sci. 13 (2022) 576–590, https://doi.org/10.1111/ijag.16566.
[10] P.P. Malik, J. Maity, Synthesis and leaching behaviour of borosilicate glasses containing uranium as radioactive waste, J Indian Chem Soc 97 (2020) 2909–2913, https://doi.org/10.5281/zenodo.5654643 fatcat:riv3a2ae6rbrjom2c32qwdsd3a.
[11] N. Praveena, H. Jena, R. Kumar, S.N. Jha, D. Bhattacharyya, S.S. Meena, Studies on the uranium speciation in zinc iron phosphate (ZnIP) glass using Mössbauer and EXAFS spectroscopic investigations, Ceram. Int. 47 (2021) 18323–18329, https://doi.org/10.1016/j.ceramint.2021.03.153.
[12] S. Gin, P. Jollivet, M. Tribet, S. Peuget, S. Schuller, Radionuclides containment in nuclear glasses: an overview, Radiochim. Acta 105 (2017) 927–959, https://doi.org/10.1515/ract-2016-2658.
[13] M. Fabian, E. Svab, T. Proffen, E. Veress, Structure study of multi-component borosilicate glasses from high-Q neutron diffraction measurement and RMC modeling, J. Non Cryst. Solids 354 (2008) 3299–3307, https://doi.org/10.1016/j.jnoncrysol.2008.01.024.
[14] R.C. Ewing, R.A. Whittleston, B.W.D. Yardley, Geological disposal of nuclear waste: a primer, Elements 12 (2016) 233–237, https://doi.org/10.2113/gselements.12.4.233.
[15] B. Grambow, Geological disposal of radioactive waste in Clay, Elements 12 (2016) 239–245, https://doi.org/10.2113/gselements.12.4.239.
[16] M.H. Bradbury, B. Baeyens, A mechanistic description of Ni and Zn sorption on Na-montmorillonite Part II: modelling, J. Contam. Hydrol. 27 (1997) 223–248, https://doi.org/10.1016/S0169-7722(97)00007-7.
[17] M.H. Bradbury, B. Baeyens, Derivation of In Situ Opalinus Clay Porewater Compositions from Experimental and Geochemical Modelling Studies, PSI Bericht Nr 97-14 (1997). ISSN 1019-0643.
[18] Z. Varga, G. Suranyi, N. Vajda, Z. Stefanka, Determination of plutonium and americium in environmental samples by inductively coupled plasma sector field mass spectrometry and alpha spectrometry, Microchemical. J. 85 (2007) 39–45, https://doi.org/10.1016/j.microc.2006.02.006.
[19] E. Svab, G. Meszaros, F. Deak, Neutron powder diffractometer at the Budapest research reactor, Mater. Sci. Forum 228-231 (1996) 247–252, https://doi.org/10.4028/www.scientific.net/msf.228-231.247.
[20] G.J. Cuello, J. Darpentigny, L. Hennet, L. Cormier, J. Dupont, B. Homatter, B. Beuneu, 7C2, the new neutron diffractometer for liquids and disordered materials at LLB, J. Phys. Conf. Ser. 746 (2016) 012020, https://doi.org/10.1088/1742-6596/746/1/012020.
[21] R.L. McGreevy, L. Pusztai, Reverse Monte Carlo simulation: a new technique for the determination of disordered structures, Mol. Simul. 1 (1988) 359–367, https://doi.org/10.1080/08927028808080958.
[22] O. Gereben, P. Jovari, L. Temleitner, L. Pusztai, A new version of the RMC++ Reverse Monte Carlo programme, aimed at investigating the structure of covalent glasses, J. Optoelectron. Adv. Mater. 9 (2007) 3021–3027.
[23] M. Fabian, P. Jovari, E. Svab, Gy. Meszaros, T. Proffen, E. Veress, Network structure of $0.7SiO_2$-$0.3Na_2O$ glass from neutron and x-ray diffraction and RMC modelling, J. Phys. Condens. Matter 19 (2007) 335209, https://doi.org/10.1088/0953-8984/19/33/335209.
[24] E. Svab, M. Fabian, E. Veress, Th. Proffen, Short- and intermediate range order in borosilicate waste glasses, Acta Crystallogr. A 61 (2007) 58–59, https://doi.org/10.1107/s0108767307098728.
[25] M. Fabian, F. Gergely, J. Osan, T. Cendak, S. Kesari, R. Rao, Structural investigation of borosilicate glasses containing lanthanide ions, Sci. Rep. 10 (2020) 7835, https://doi.org/10.1038/s41598-020-64754-2.
[26] A.J. Dent, G. Cibin, S. Ramos, A.D. Smith, S.M. Scott, L. Varandas, M.R. Pearson, N. A. Krumpa, C.P. Jones, P.E. Robbins, B18: a core XAS spectroscopy beamline for Diamond, J. Phys. Conf. Ser. 190 (2009) 012039, https://doi.org/10.1088/1742-6596/190/1/012039.
[27] G.K. Liu, H.Z. Zhuamg, J.V. Beitz, J.W. Williams, V.S. Vikhnin, Structure and charge transfer dynamics of uranyl ions in boron oxide and borosilicate glasses, Phys. Solid State 44 (2002) 1433–1439, https://doi.org/10.1134/1.1501332.
[28] M. Newville, EXAFS analysis using FEFF and FEFFIT, J. Synchrot. Rad 8 (2001) 96–100, https://doi.org/10.1107/S0909049500016290.
[29] Standard test methods for determining chemical durability of nuclear, hazardous, and mixed waste glasses and multiphase glass ceramics: the product consistency test (PCT) 2021. 10.1520/C1285-21.
[30] A. Varga, B. Raucsik, G. Szakmany, Z. Mathe, Mineralogical, petrological and geochemical characteristics of the siliciclastic rock types of Boda Siltstone Formation, Foldtani Kozlony 136 (2006) 1–31.
[31] S. Vaishnav, A.C. Hannon, E.R. Barney, P.A. Bingham, Neutron diffraction and raman studies of the incorporation of sulfate in silicate glasses, J. Phys. Chem. C 124 (2020) 5409–5424, https://doi.org/10.1021/acs.jpcc.9b10924.
[32] A.C. Hannon, S. Vaishnav, O.L.G. Alderman, P.A. Bingham, The structure of sodium silicate glass from neutron diffraction and modeling of oxygen-oxygen correlations, J. Am. Ceramic Soc. 104 (2021) 6155–6171, https://doi.org/10.1111/jace.17993.
[33] S. Urakawa, T. Inoue, T. Hattori, A. Sano-Furukawa, S. Kohara, D. Wakabayashi, T. Sato, N. Funamori, K. Funakoshi, X-ray and neutron study on the structure of hydrous SiO_2 glass up to 10 GPa, Minerals 10 (1) (2020) 84, https://doi.org/10.3390/min10010084.
[34] N. Ohtori, K. Takase, I. Akiyama, Y. Suzuki, K. Handa, I. Sakai, Y. Iwadate, T. Fukunaga, N. Umesaki, Short-range structure of alkaline-earth borate glasses by pulsed neutron diffraction and molecular dynamics simulation, J. Non. Cryst. Solids. 293-295 (2001) 136–145, https://doi.org/10.1016/S0022-3093(01)00662-7.
[35] A.K. Connelly, N.C. Hyatt, K.P. Travis, R.J. Hand, M.C. Stennett, A.S. Gandy, A. P. Brown, D.C. Apperley, The effect of uranium oxide additions on the structure of alkali borosilicate glasses, J. Non. Cryst. Solids. 378 (2013) 282–289, https://doi.org/10.1016/j.jnoncrysol.2013.06.026.
[36] A.E. Burns, D.W. Winslow, W.J. Clarida, M. Affatigato, S.A. Feller, R.K. Brow, Structure of binary neodymium borate glasses by infrared spectroscopy, J. Non. Cryst. Solids. 352 (2006) 2364–2366, https://doi.org/10.1016/j.jnoncrysol.2006.03.043.
[37] M. Fabian, E. Svab, M. von Zimmermann, Structure study of new uranium loaded borosilicate glasses, J. Non. Cryst. Solids. 380 (2013) 71–77, https://doi.org/10.1016/j.jnoncrysol.2013.09.004.
[38] S.V. Stefanovsky, A.A. Shiryaev, J.V. Zubavitchus, A.A. Veligjanin, J.C. Marra, Valence state and speciation of uranium ions in borosilicate glasses with a high iron and aluminum content, Glass Phys. Chem. 35 (2009) 141–148, https://doi.org/10.1134/S1087659609020035.
[39] S. Farges, C.W. Ponader, G. Calas, G.E. Brown Jr, Structural environments of incompatible elements in silicate glass/melt systems: II. UIV, UV, and UVI, Geochim. Cosmochim. Acta 56 (1992) 4205–4220, https://doi.org/10.1016/0016-7037(92)90261-g.
[40] M. Fabian, T. Proffen, U. Ruett, E. Veress, E. Svab, Uranium surroundings in borosilicate glass from neutron and x-ray diffraction and RMC modelling, J. Phys. Condensed Matter 22 (2010) 404206, https://doi.org/10.1088/0953-8984/22/40/404206.

[41] N.M. Vedishcheva, B.A. Shakhmatkin, A.C. Wright, The structure of sodium borosilicate glasses: thermodynamic modelling vs. experiment, J. Non. Cryst. Solids. 345-346 (2004) 39–44, https://doi.org/10.1016/j.jnoncrysol.2004.07.040.
[42] M. Fabian, E. Svab, T. Proffen, E. Veress, Neutron diffraction and reverse Monte Carlo modelling of v-B_2O_3 and $75B_2O_3$-$25Na_2O$ glasses, J. Non. Cryst. Solids. 356 (2010) 441–446, https://doi.org/10.1016/j.jnoncrysol.2009.12.013.
[43] L. Cormier, D.R. Neuville, Ca and Na environments in Na_2O-CaO-Al_2O_3-SiO_2 glasses: influence of cation mixing and cation-network interactions, Chem. Geol 213 (2004) 103–113, https://doi.org/10.1016/j.chemgeo.2004.08.049.
[44] T. Taniguchi, M. Okuno, T. Matsumoto, X-ray diffraction and EXAFS studies of silicate glasses containing Mg, Ca and Ba atoms, J. No n Cryst. Solids 211 (1997) 56–63, https://doi.org/10.1016/s0022-3093(96)00632-1.
[45] L.B. Skinner, A.C. Barnes, W. Crichton, Novel behaviour and structure of new glasses of the type Ba-Al-O and Ba-Al-Ti-O produced by aerodynamic levitation and laser heating, J. Phys. Condensed Matter 18 (2006) L407, https://doi.org/10.1088/0953-8984/18/32/L01.
[46] C. Meneghini, A.F. Gualtieri, C. Siligardi, Differential anomalous wide-angle X-ray scattering and X-ray absorption experiments to investigate the formation of glass ceramics in the CaO-SiO_2-ZrO_2 system, J Appl Cryst 32 (1999) 1090–1099, https://doi.org/10.1107/S0021889899010675.
[47] G. Ferlat, L. Cormier, M.H. Thibault, L. Galoisy, G. Calas, J.M. Delaye, D. Ghaleb, Evidence for symmetric cationic sites in zirconium-bearing oxide glasses, Phys. Rev. B 73 (2006) 214207, https://doi.org/10.1103/PhysRevB.73.214207.
[48] L.S. Du, J.F. Stebbins, Solid-state NMR study of metastable immiscibility in alkali borosilicate glasses, J. Non. Cryst. Solids. 315 (2003) 239–255, https://doi.org/10.1016/S0022-3093(02)01604-6.
[49] M. Fabian, Cs. Araczki, Basic network structure of SiO_2-B_2O_3-Na_2O glasses from diffraction and reverse Monte Carlo simulation, Phys. Scr. 91 (2016) 054004, https://doi.org/10.1088/0031-8949/91/5/054004.
[50] N. Praveena, H. Jena, S. Bera, R. Kumar, S.N. Jha, D. Bhattacharyya, Studies on chemical state of uranium in modified sodium borosilicate glass using X-ray photoelectron spectroscopy and X-ray absorption spectroscopy, Progress Nuclear Energy 131 (2021) 103579, https://doi.org/10.1016/j.pnucene.2020.103579.
[51] A. Shiryaev, Z.V. Zubavichus, Article in glass technology, European J. Glass Sci. Techn. Part A 50 (2009) 1. Available online: http://www.ingentaconnect.com.
[52] N. Praveena, J. Hrudananda, M.R. Sankaran, Studies on the effect of uranium loading on the glass transition temperature (T_g) of borosilicate glass containing oxides of ca, ti and al for the immobilization of radwaste, in: ISMC-2018 Conference Paper Mumbai, India A-147, 2021, pp. 1–2.
[53] T. Maeda, T. Banba, K. Sonoda, Y. Inagaki, H. Furuya, Release and retention of uranium during glass corrosion, J. Nuclear Mater. 298 (2001) 163–167, https://doi.org/10.1016/S0022-3115(01)00587-6.
[54] V.S. Thorat, R.K. Mishra, S.V. Kumaran, A. Kumar, R.K. Vatsa, C.P. Kaushik, A. K. Tyagi, Corrosion of borosilicate glasses subjected to aggressive test conditions: structural investigations, J. Am. Ceramic Soc. 99 (2016) 3251–3259, https://doi.org/10.1111/jace.14340.
[55] L.T. Chen, X.T. Ren, Y.N. Mao, J.J. Mao, X.Y. Zhang, T.T. Wang, M.L. Sun, T. S. Wang, M.M. Smedskjaer, H.B. Peng, Radiation effects on structure and mechanical properties of borosilicate glasses, J. Nuclear Mater. 552 (2021) 153025, https://doi.org/10.1016/j.jnucmat.2021.153025.